

# Multi-Objective Shape Optimization Study for a Subsonic Submerged Inlet

Ezgi S. Taskinoglu\* and Doyle D. Knight†  
Rutgers University, Piscataway, New Jersey 08854-8058

The findings of a multi-objective shape optimization study conducted for a subsonic submerged air vehicle inlet are summarized. The objective functions of the optimization problem are distortion and swirl indices defined by the distribution of flow parameters over the exit cross section of the inlet. The geometry alteration is performed by placing a protrusion in the shape of a fin on the baseline inlet surface. Therefore, the design variables of the optimization problem are chosen to be the geometrical parameters defining the fin protrusion, namely, fin height, length, and incidence angle. The trade-off (also known as the  $\varepsilon$ -constraint) method is employed for finding the Pareto optimal set formed by the nondominated solutions of the feasible design space. Because the flow-domain solution is required for every step along the line search, an automated optimization loop is constructed by integrating the optimizer with a surface modeler, a mesh generator, and a flow solver through which the flow parameters over the compressor face are computed. In addition, the trade study for fin protrusion, and the analyses and the comparison of the baseline and Pareto optimal solutions are presented, and observations concerning grid resolution and convergence behavior are discussed.

## Nomenclature

$DC(\phi)$	=	distortion index
$f(x)$	=	objective function
$g(x)$	=	constraint function
$h_{fin}$	=	height of the fin protrusion, m
$l_{fin}$	=	length of the fin protrusion, m
$M$	=	Mach number
$p$	=	pressure, Pa
$q$	=	dynamic head
$R$	=	exit cross section radius of the inlet, m
$r$	=	radial body axis, m
$SC(\phi)$	=	swirl index
$T$	=	temperature, K
$U$	=	axial velocity, m/s
$v_\theta$	=	crossflow velocity, m/s
$x, y, z$	=	Cartesian body axes, m
$\mathbf{x}$	=	Design variables, $x_k, k = 1, 2, 3, \dots$
$\alpha$	=	angle of attack
$\beta$	=	angle of sideslip
$\gamma_{fin}$	=	incidence angle of the fin protrusion, deg
$\delta$	=	boundary-layer thickness
$\varepsilon$	=	user-defined constraint values
$\theta$	=	azimuthal body axis, deg
$\rho$	=	density, kg/m <sup>3</sup>
$\phi$	=	angular width of region for $DC$ and $SC$ , deg

## Subscripts

0	=	stagnation values
$\infty$	=	freestream

Received 14 October 2003; revision received 23 January 2004; accepted for publication 23 January 2004. Copyright © 2004 by Ezgi S. Taskinoglu and Doyle D. Knight. Published by the American Institute of Aeronautics and Astronautics, Inc., with permission. Copies of this paper may be made for personal or internal use, on condition that the copier pay the \$10.00 per-copy fee to the Copyright Clearance Center, Inc., 222 Rosewood Drive, Danvers, MA 01923; include the code 0748-4658/04 \$10.00 in correspondence with the CCC.

\*Graduate Student, Department of Mechanical and Aerospace Engineering, 98 Brett Road. Member AIAA.

†Professor, Department of Mechanical and Aerospace Engineering, 98 Brett Road. Associate Fellow AIAA.

## Introduction

THE component of the air vehicle from which atmospheric air is delivered to a turbojet or ramjet engine is called the inlet (or intake). It is basically a fluid flow duct through which the incoming freestream air is retarded to convert kinetic energy into pressure. The engine thrust depends on this pressure value of the airflow at the entrance of the compressor or ramjet combustor. Although the inlet does no work on the flow itself, it is responsible for processing the airflow in such a way to ensure engine operability, which requires high quality of the air at the face of the engine. The term high-quality airflow refers to the optimum levels of total pressure and flow uniformity that are vital for engine operability and stability. The maldistribution of the airflow entering the engine in terms of total pressure variation over the inlet discharge is called flow distortion. It degrades the total pressure recovery and lowers the surge line limiting the engine operability conditions. The measure of flow angularity to the duct centerline is called flow swirl. Flow distortion and swirl are required to be lower than certain values to provide compatibility between the inlet and the engine. Hence, inlet designers aim to achieve maximum possible efficiency while keeping the uniformity of the flow at the compressor entry above a certain level, which is engine specific.<sup>1–4</sup>

The necessity of reducing the overall weight of an air vehicle leads to short ducts and highly curved hump inlets. In these designs, the shape of the inlet, because it has an off-center curvature or variation in cross-sectional area or out-of-plane bends, yields cross stream pressure gradients, which in turn produce secondary flows along the walls leading to flow separation and nonuniform velocity.<sup>5–8</sup> For example, a submerged (also known as flush-mounted or tunnel) inlet is an attractive inlet design that can achieve lower drag, weight, and radar cross section compared to a conventional nacelle-mounted inlet. However, the efficiency and flow uniformity of a submerged inlet is highly dependent on the boundary layer ingested into the inlet. This type of inlet is only favorable in a region of thin boundary layer, in other words when it is placed in the forward section of the body.<sup>9,10</sup>

There are several methods to minimize the flow nonuniformity. One method is to avoid and/or to control the incoming boundary layer. This can be accomplished by raising the inlet above the boundary layer and plow the boundary layer around the inlet.<sup>11</sup> Alternatively, the boundary layer can be removed by placing slots and holes just ahead of the inlet station and/or can be reenergized by blowing air. Boundary-layer suction, blowing, and their combination have been shown to lower the flow distortion by minimizing the

separation in the inlet duct.<sup>12</sup> Another method of reenergizing the boundary layer is to locate surface protrusions, called vortex generators, within the boundary near the entrance of the diffuser.<sup>6,13–15</sup> These are small wing sections sized to the local boundary-layer height and mounted upstream of the problem area. The vortex generators are usually used in groups of two or more, and they are inclined at an angle to the oncoming flow to generate a shed vortex that will induce mixing between the core flow and the low-energy boundary-layer flow. Aerodynamic grid is one other method to control flow distribution. This forced-mixing device can be in different forms: holes, spokes, or annular rings. It is placed at the inlet discharge to reduce the distortion by redistributing the energy of the flow at the expense of the mean total pressure.<sup>2,11</sup> A spoiler consisting of a vertical strip fitted inside the lip of an S-duct diffuser is found to reduce the swirl.<sup>2,16</sup> Fences placed in the first bend of an S-duct diffuser on the centerlines of the lower and outside walls have been found to resolve the flow swirl problem<sup>2,17</sup> as well.

An alternative method of minimizing exit flow distortion is to employ shape optimization. Automated shape optimization, that is, coupling computational fluid dynamics software with an optimization algorithm to determine better design shapes under several constraints, became a powerful design tool with the advent of powerful computers and advanced technologies.<sup>18</sup> Automated design optimization includes two main components: a design associate (DA) and a modeling and simulation associate (MSA). The DA corresponds to the optimizer that is the control mechanism of the design process. The MSA is composed of a geometry module, a grid-generation module, a flow solver module, and a postprocessor module. Function evaluation at each iteration of the design optimization process is done by the MSA. It is invoked by the DA in an iterative loop until the prescribed design criteria are met.<sup>19</sup> There are several optimization methodologies. Steepest descent, conjugate gradient, and sequential quadratic programming are examples of gradient-based optimization techniques. They share the common limitation of being trapped in a local minimum rather than finding the global optimum. Stochastic optimization methods, on the other hand, incorporate a measure of randomness in the optimization process to avoid convergence to a local minimum. Simulating annealing and genetic algorithms are examples of these kind of methods. However, they require substantially more iterations than gradient-based algorithms.

A summary of the studies performed on the design optimization for high-speed inlets can be found by Knight.<sup>20</sup> Zha et al. optimized an axisymmetric mixed compression ramjet inlet at Mach 4 and 18.3-km altitude.<sup>21</sup> The objective of the design was to maximize total pressure recovery. The feasible design space was defined by the constraints imposed by engine operability, structural integrity, and manufacturing and geometrical parameters. Blaize and Knight<sup>22</sup> and Blaize et al.<sup>23</sup> employed a single-objective algorithm to maximize the total pressure recovery of a two-dimensional missile inlet for a single flight point and an entire mission. Blaize and Knight used GADO<sup>24</sup> and obtained 20–30% improvement in total pressure recovery. It is concluded in this study that in a short period of time it is possible to achieve improved inlet designs through the use of automated design optimization.<sup>22</sup> Repeating the same design optimization loop for the entire mission indicated that this powerful and innovative search process is capable of finding better inlet designs for specific missions with higher efficiency than conventional methods.<sup>23</sup> A similar design methodology for a three-dimensional supersonic inlet was performed to achieve maximum total pressure recovery at a single flight condition.<sup>25,26</sup> For S-duct subsonic diffusers, a Gaussian bump located upstream of the separation region showed an improvement for flow distortion at the exit plane.<sup>27</sup> This study was accomplished by an automated design optimization in which a design loop was constructed by linking a flow solver with an optimizer to optimize the S-shaped subsonic diffuser shape.<sup>27,28</sup> Zhang et al.<sup>27</sup> explained the performance improvement seen in the diffuser by the suppression of detrimental secondary flows as a result of surface modification which redirected the flow. Lefantzi and Knight<sup>28</sup> emphasized the complex three-dimensional flow separation in the bump by means of flowfield visualizations.

This paper presents an automated shape optimization study for a submerged inlet using a gradient-based optimizer. The objective functions of the optimization problem are selected to be distortion and swirl indices defined over the inlet discharge. The geometry of the baseline inlet is altered by introducing a surface protrusion in the shape of a fin at the duct bend region around the centerline of the duct side walls.

### Problem Statement

The generic air vehicle analyzed in this study is shown in Fig. 1a. It is simply an ogive cylinder with a humped curved diffuser. The coordinates of the conic nose of the air vehicle are given parametrically as follows:  $x = 64.18t^2 + 7.13t^3$  and  $y = 21.34t + 33.53t^2 - 29.47t^3$ , where  $0 < t < 1$ . A closeup view of the diffuser is shown in Fig. 1b. The dimensions are in millimeters in both Figs. 1a and 1b. The inlet is a compact diffuser flush with the fuselage and small compared to the air vehicle. Its entry is submerged within the general contour of the body. It has a long gently sloping ramp that increases the flow speed as it enters to the inlet.

### Objective Functions

Our figures of merit in this study are flow distortion and swirl at the engine face. Both are defined over the exit cross section of the inlet channel (Fig. 2). The distortion index is the maximum deviation of the average total pressure in the pie-shaped sector of angular size  $\psi$  from the mean total pressure over the entire exit cross section of radius  $R$ . It is defined as follows:

$$DC(\phi, \psi) = \max\{[\bar{p}_0 - \bar{p}_0(\phi, \psi)]/\bar{q}\}, \quad 0 < \phi \leq 2\pi \quad (1)$$

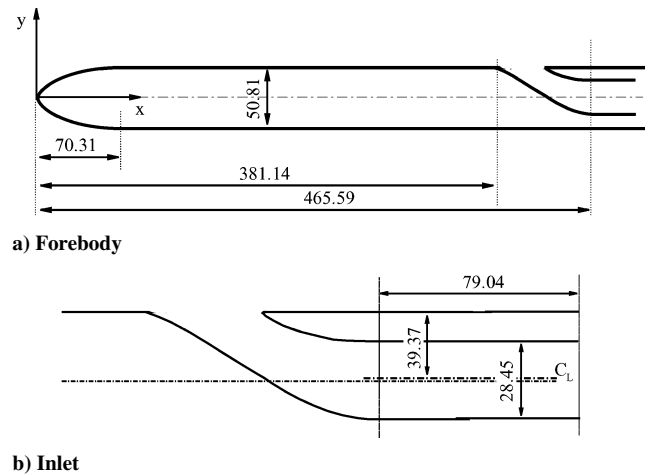


Fig. 1 Forebody and inlet configuration (dimensions in millimeters).

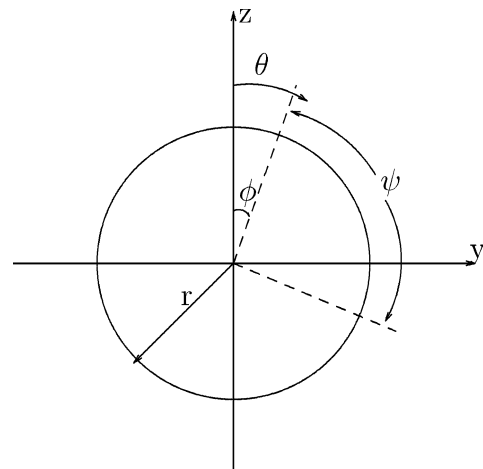


Fig. 2 Two-dimensional exit cross section of the inlet channel.

where  $p_0$  is the total pressure,  $q$  is the dynamic pressure, and  $\phi$  is the starting angle for a pie-shaped segment of angle  $\psi$  radians of the diffuser exit. It is

$$\bar{p}_0 = \frac{\int_0^{2\pi} \int_0^R p_0(r, \theta) r dr d\theta}{\int_0^{2\pi} \int_0^R r dr d\theta}$$

$$\bar{p}_0(\phi, \psi) = \frac{\int_0^\psi \int_0^R p_0(r, \phi + \theta) r dr d\theta}{\int_0^\psi \int_0^R r dr d\theta}$$

$$\bar{q} = \frac{\int_0^{2\pi} \int_0^R q r dr d\theta}{\int_0^{2\pi} \int_0^R r dr d\theta}$$

The swirl index is the maximum average circumferential crossflow velocity in an angular sector of size  $\psi$ , nondimensionalized by the mean axial velocity at the exit cross section. It is defined as follows:

$$SC(\phi, \psi) = \max\{[\bar{v}_\theta(\phi, \psi)]/\bar{U}\}, \quad 0 < \phi \leq 2\pi \quad (2)$$

where  $v_\theta$  is the circumferential crossflow velocity,  $\bar{U}$  is the mean axial velocity over the exit cross section, and  $\phi$  is the starting angle for a pie-shaped segment of angle  $\psi$  of the diffuser exit. It is

$$\bar{v}_\theta(\phi, \psi) = \frac{\int_0^\psi \int_0^R v_\theta(r, \phi + \theta) r dr d\theta}{\int_0^\psi \int_0^R r dr d\theta}$$

$$\bar{U} = \frac{\int_0^{2\pi} \int_0^R U r dr d\theta}{\int_0^{2\pi} \int_0^R r dr d\theta}$$

Zhang et al.<sup>27</sup> found that distortion index behavior is similar for different pie segment angles. Thus, in our study only one distortion index is taken into consideration,  $\psi = 45$  deg.

### Multi-Objective Optimization

The purpose of this study is to minimize both flow distortion and swirl for a subsonic submerged air vehicle inlet as mentioned in the preceding section. For this purpose, a computer aided design (CAD) model of a generic submerged inlet was created (Fig. 3). Then, its geometry is altered and for every geometry alteration, the flow physics around the inlet is numerically analyzed. This two-step process, creating the geometry and analyzing the flow domain, is repeated in successive iterations to obtain better inlet design geometries. However, rather than a random choice, every new inlet design is selected through a control mechanism over a specified range of inlet geometries. This control mechanism refers to the optimizer, and the set of possible inlet geometries defines the design space of the shape optimization problem.

Having two objective functions, flow distortion and flow swirl, our optimization problem is an example of a multi-objective or multi-criteria decision-making problem. Most of the design problems in

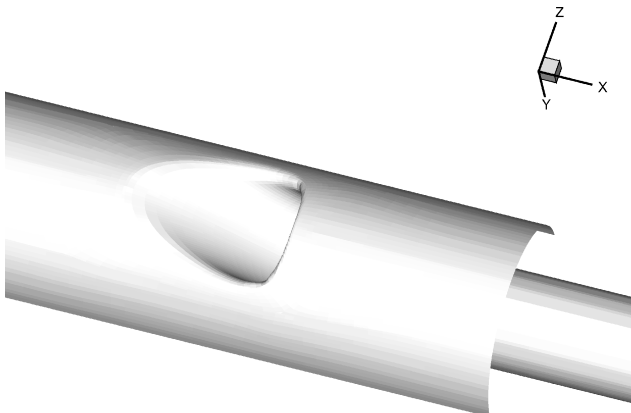
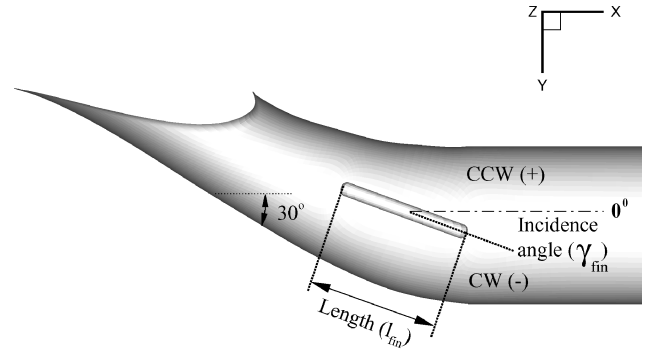
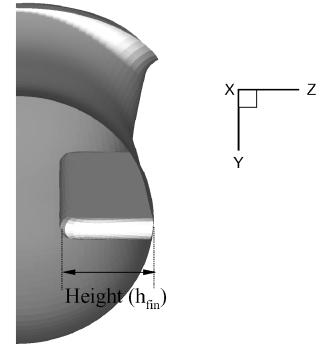


Fig. 3 Generic inlet.



a) Side view



b) View looking upstream

Fig. 4 Design variables for a fin type of deformation.

engineering have several objectives. These objectives can be conflicting with one another. Therefore, rather than finding one single solution, a set of good compromises are sought. The decision maker searches for the values of design variables  $\mathbf{x} = (x_1, \dots, x_k)$ , which optimize the objective functions  $f_i, i = 1, 2, \dots, m$ , simultaneously. Because a vector of design variables that are acceptable by the decision maker is searched, this type of optimization problem is also known as vector optimization. The set of solutions from which the decision maker selects the desired values of design variables is called the Pareto-optimal set (see Ref. 29). A set of points  $\mathbf{x}^*$  is Pareto optimal if there exists no feasible vector of design variables that would decrease any one of the objective functions without causing a simultaneous increase at least in one other objective function. The vectors  $\mathbf{x}^*$  corresponding to the solutions included in the Pareto optimal set are called nondominated. A design  $\mathbf{x}_a$  is dominated by a design  $\mathbf{x}_b$  if  $f_i(\mathbf{x}_b) \leq f_i(\mathbf{x}_a)$ , for  $i = 1, \dots, k$ , and for at least one value of  $i$ ,  $f_i(\mathbf{x}_b) < f_i(\mathbf{x}_a)$ , where  $k$  is the dimension of vector  $\mathbf{x}$ . The set of nondominated designs is the Pareto set. The plot of the objective functions whose nondominated vectors are in the Pareto set is called the Pareto front.

### Design Variables

A trade study for a wide range of possible geometric deformations of the baseline geometry was performed. According to this trade study, deformation in the shape of a fin (Fig. 4) over the inlet channel was found to be promising for achieving a lower distortion and/or swirl index at the exit cross section of the channel. Therefore, the design variables of the optimization process, namely,  $\mathbf{x} = (x_1, x_2, x_3)$ , are chosen to be the height  $h_{fin}$ , the length  $l_{fin}$ , and the angle of incidence of the fin,  $\gamma_{fin}$ , respectively (Fig. 4).

### Optimization Methodology

The objective, constraint, and gradient definitions for our design problem are not explicit functions of the design variables. Hence, rather than hard coding the implicit definitions into the optimizer, a function evaluation algorithm outside of the optimizer must be used. This requires output of the design variable values from the optimizer and input of objective, constraint and gradient values into

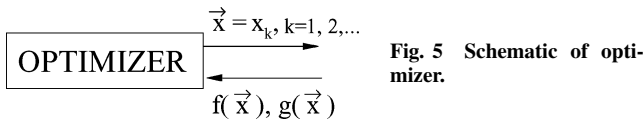


Fig. 5 Schematic of optimizer.

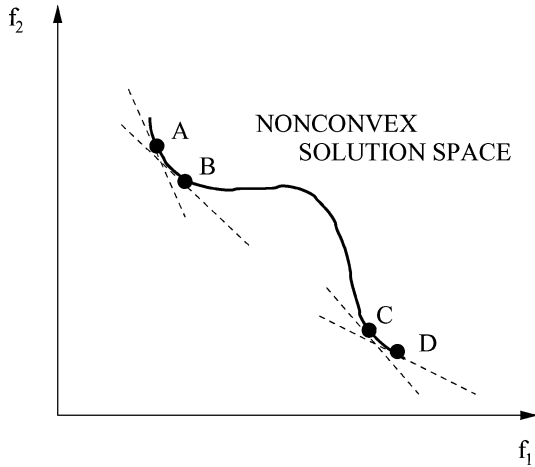


Fig. 6 Schematic of weighted sum approach.

the optimizer. A schematic representation of the use of an optimizer is given in Fig. 5. Here,  $x_k$  refers to the  $k$  design variables  $\mathbf{x} = (x_1, x_2, x_3)$ , and  $f(\mathbf{x})$  and  $g(\mathbf{x})$  refer to corresponding objective and constraint functions, respectively.

Multi-objective optimization problems can be treated as single-objective problems by scalarizing the objective vector into a single objective. There are different methods available in the literature for scalarization of the objective functions. Before the presented research, an optimization study based on the weighted sum approach<sup>29</sup> was performed for the solution of a similar inlet shape optimization problem.<sup>30</sup> In this approach, the composite function is defined by minimizing the composite function for a set of weight parameters called a weight vector. Every choice of weight vector represents a contour line, Pareto solutions are formed from the tangent points of these contour lines with the feasible solution space. Because in the nonconvex region contour lines before being tangent to the solution space meet with the tangent points on the edges of the objective space (either point B or C in Fig. 6), the weighted sum approach fails to find Pareto-optimal solutions in the nonconvex region (region between points B and C in Fig. 6). Thus, this approach can not find entire Pareto set in the case of nonconvex solution space.<sup>31</sup> Our optimization study performed by the weighted sum approach yielded an irregular and discontinuous Pareto set, indicating the possibility of nonconvex solution space. Hence, in the presented study due to the possible nonconvex nature of our problem, we employed the trade-off (also known as  $\varepsilon$ -constraint) technique.<sup>29</sup> The trade-off method is not biased toward the convex portions of the Pareto set, that is, it is able to find solutions associated with the nonconvex part of the Pareto front. It selects only one objective function to minimize. Other objective functions are restricted with user-specified values. Hence, the problem with many objectives is transferred into a single objective problem with an additional set of constraints. A schematic representation of the method is shown in Fig. 7. Because there is one constraint  $\varepsilon_1$  that divides the feasible solution space as shown in Fig. 7, the optimization problem becomes the minimization of  $f_2$ , whereas  $f_1 < \varepsilon_1$ . Clearly, the solution is point B. In this way, the nonconvex feasible solution domain can be divided into several subdomains for which a new optimization problem is to be solved, and a new design point on the Pareto set is to be found. Hence, to determine the complete Pareto set, the user-defined  $\varepsilon$  values are varied. It is critical to specify a valid range of the  $\varepsilon$  values to avoid empty solution sets. The number of constraints will decide the number of single-objective optimization problems. Figure 8 shows a schematic representation of the optimization algorithm based on

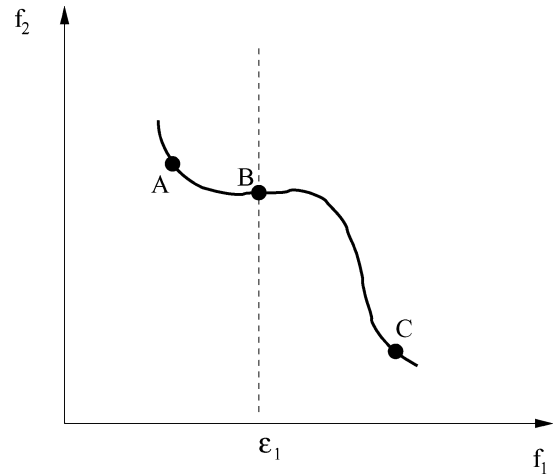


Fig. 7 Schematic of trade-off method.

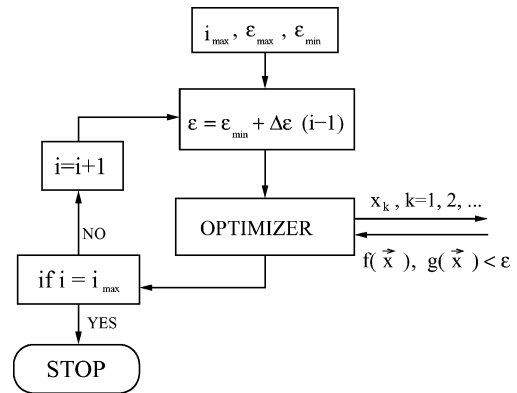


Fig. 8 Schematic of optimization based on trade-off method.

the trade-off method. The number of optimization runs ( $i_{\max}$  in the Fig. 8) is problem dependent. In our problem, the distortion index is being minimized while the swirl index is constrained. We selected 12 different  $\varepsilon$  values between the maximum (0.300) and the minimum (0.025) swirl index range. For each predefined  $\varepsilon$  value, a new optimization for the distortion index is performed while the swirl index is constrained.

The distortion and swirl indices are calculated from the total pressure and crossflow velocity distribution, respectively, over the compressor face by means of an auxiliary postprocessor. This program requires the distribution of the primitive flow variables, namely, the density, velocity, and pressure, over the exit of the inlet channel as an input. Hence, the flow domain of the inlet is required to be solved for each time the design variable values are changed. Consequently, it becomes necessary to construct an optimization loop by integrating the optimizer (DA) with a surface modeler, a mesh generator, a flow solver, and an auxiliary postprocessor (MSA) (Fig. 9).

### Components of the Optimization Loop

The design loop of our specific application is given in Fig. 9. A third party software, namely, CFSQP<sup>32</sup> is employed as an optimizer. Pro/Engineer,<sup>33</sup> developed by Parametric Technology, Inc., is chosen to be the geometry modeler. GridPro,<sup>34</sup> developed by Program Development Corporation, is utilized for mesh generation. GASPex,<sup>35</sup> developed by Aerosoft, Inc., is the flow solver. The auxiliary program DC/SC is used for postprocessing the flow domain solution to evaluate the objective function value.

### Optimizer: CFSQP

CFSQP is a gradient-based optimizer that requires the objective functions, the design variables, and the feasible set of design points in the form of constraint definitions to be supplied by the user.

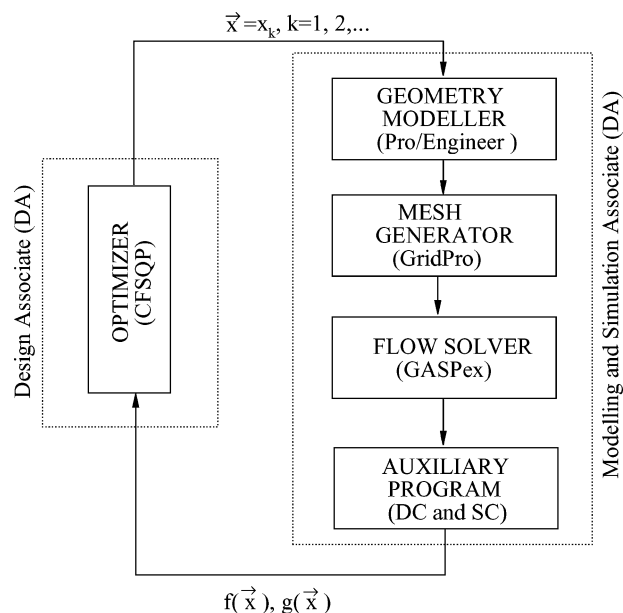


Fig. 9 Design loop.

It is optional to supply respective gradient information or to let CFSQP estimate them by forward or centered finite differences. Our design optimization methodology is an iterative process having two main steps: 1) obtaining the new estimate for the design variables  $x_k$ ,  $k = 1, 2, \dots$ , and 2) calculating the corresponding objective function value  $f(x)$  at each iteration. These two steps are repeated until the stopping criteria is met, that is, until either the optimum value is obtained or the maximum number of iterations is exceeded. The optimizer decides either to end the process according to the user-supplied stopping criterion or to select the new iterate. The inputs of the program, thus, are the objective and constraint functions  $f(x)$  and  $g(x)$ , respectively. The intermediate outputs are new design variable estimates, which finally give optimum values at the end of the program.

#### Surface Modeler: Pro/Engineer

In this study, solid modeling for the baseline geometry and the surface alteration in the form of a fin are generated by the CAD program Pro/Engineer, release 20 (Ref. 33). The alteration of the surface protrusion is done by means of the macrofile created with the parametric definitions of the design variables. Once this file for one specific set of design variables is ready, changing the shape of the fin is simply overwriting it for every other set. The input for Pro/Engineer is the design variable set constructed by every new iterates of CFSQP. The output is the surface mesh of the new design prepared in NASTRAN format.

#### Mesh Generator: GridPro

GRIDPRO/az3000 (Ref. 35) is a general purpose elliptic mesh generator that creates a three-dimensional, multiblock structured grid by a variationally based method with an iterative updating scheme. The user inputs for GRIDPRO are the surface geometry and the block topology. Note that the same topology definition is used during the optimization while the surface definition changes. After the grid for the inviscid flow analysis is obtained, clustering near the wall region can be achieved by specifying the first cell height and the stretching ratio.

#### Flow Solver: GASPex

The flow solver used is GASPex, version 4.1.+ (Ref. 35), which solves the Reynolds averaged compressible time-dependent Navier–Stokes equations in three dimensions. It utilizes a finite volume spatial discretization in which the state variables are stored at the cell centers. The accuracy of reconstructing the primitive variable field at the cell faces determines the spatial accuracy of the solution.

Table 1 Flow conditions

Condition	Value
Pressure $p_\infty$ , kPa	99.75
Density $\rho_\infty$ , kg/m <sup>3</sup>	1.21
Temperature $T_\infty$ , K	287.26
Mach number $M_\infty$	0.15
Angle of attack $\alpha$	0.00
Angle of sideslip $\beta$	0.00
Incoming boundary-layer thickness $\delta$ , mm	8.00

The MUSCL approach is performed for variable extrapolation. In our computations, the inviscid flux scheme is Roe's method with third-order spatial accuracy reconstruction using the Min Mod limiter. Turbulence is modeled by the Wilcox  $k-\omega$  model. A steady-state solution is obtained by applying the Gauss–Seidel relaxation scheme.

Inflow boundary conditions are prepared from the numerical solutions of the axisymmetric forebody upstream of the inlet. As an outflow boundary condition, a back pressure of 99.75 kPa (equal to the freestream static pressure) is specified at the exit of the diffuser. Dimensions of the baseline inlet are approximately half of a typical cruise missile due to the constraints imposed by the experimental setup. The flow conditions are indicated in Table 1. They were selected to permit a subsequent experimental study in Rutgers University Low Speed Tunnel. Although the flow speed is substantially lower than a typical cruise missile, the objective of the study is the development and validation of the design optimization methodology, which can be extended to higher flight speeds in subsequent studies.

#### Auxiliary Postprocessor: DC/SC

Once the flow-domain solution is obtained, the dataset at the exit cross section is processed to compute the distortion and swirl indices. Postprocessing consists of the following steps. First, a triangular mesh of the exit cross section as a whole is created. Second, the mean total pressure is calculated by adding the average of flow parameters for each cell. Third, the exit cross section is divided into pie segments, and mean total pressure for each segment is calculated. Fourth, the maximum deviation from the mean total pressure is computed and nondimensionalized by the mean dynamic head to obtain the distortion index. To find the swirl index, the same procedure is used, this time, for calculation of the mean crossflow velocity. The maximum deviation from the mean cross velocity is nondimensionalized by the mean axial velocity to obtain swirl index.

#### Interfaces Between Components

There are two loops in our optimization strategy. The first loop is necessary to scalarize the multi-objective optimization problem. In other words, instead of an optimization process having a vector of optimum solutions, we have a vector of optimization problems with one solution of each. Every problem is solved one at a time successively. Each successive run is started in an automated way through a mechanism that changes the problem definition according to the new constraint value of  $\epsilon$ . Before this mechanism is launched, the user must specify a meaningful range of  $\epsilon$  values and the number of optimization problems. This mechanism is constructed outside of the optimizer by means of a PERL script,<sup>36</sup> which simply alters the constraint definition in the optimization problem for every new  $\epsilon$  value.

The function evaluation process necessitates the second loop. It is driven by the optimizer as many times as is required to obtain the solution for that specific problem. Thus, for each optimization problem, it is invoked a number of times determined by the optimizer as a module of the first loop. Building the second loop is, in fact, assembling the software components in such a way as to enable communication among them. Each component provides information to and requires other information from the other components. Therefore, a second mechanism that starts the successive runs of

each component while preparing the information needed for the current job and transferring the information necessary for the next job is constructed. Similar to first mechanism, the PERL script language is used for this mechanism. Note that the optimization loop uses different computers with different architectures due to the requirements of the individual software packages and/or need for substantial computational resources. For example, Pro/Engineer is not available for the Linux operating system, although the CPU intensive part of our problem, that is, the flow solver, is executed on a Linux cluster.

## Results

The analysis of the inlet includes solution of the external flow over the entire air vehicle and the internal flow inside the diffuser duct. The long forebody upstream of the diffuser duct is an axisymmetric ogive cylinder. Its geometry was not altered during the optimization process. Therefore, to speed up the design optimization process, the flow domain is split into two parts, namely, the forebody section and the channel section (Fig. 10). The forebody section is the axisymmetric body upstream of the inlet opening and has an overlapped region with the channel section that includes the inlet duct. In our design optimization study, we solve the forebody section only once and we implement its solution as a pointwise inflow boundary condition for the channel section.

### Baseline Inlet

#### Part 1

Numerical simulations for the baseline submerged inlet have been performed for the freestream conditions given in Table 1. The forebody section convergence is reached in 42,000 steps. Computations are presented in Figs. 11a and 11b. In Fig. 11a, the variation in skin-friction coefficient along the solid wall is shown. In Fig. 11b, the velocity profile at the end of the first domain can be seen. The forebody section is approximately equivalent to a flat plate, because the ratio of the boundary-layer thickness to the diameter is small, that is, curvature effects are small, and the distance from the vehicle nose to the inlet is large compared to the length of the curved portion of the forebody. Therefore, flat plate boundary-layer approximation formulas will be utilized to verify the computational results. At Reynolds numbers above  $3 \times 10^5$ , the boundary layer on a flat plate is turbulent except for a small region near the leading edge. Examination of Fig. 11b yields the computed boundary-layer thickness to be 8 mm, which is comparable with the predicted value from a flat plate boundary-layer analysis at  $x = 0.25$  m. The boundary-layer thickness at this location is predicted to be 8.4 mm by using flat plate formulations. Similarly, the skin-friction coefficient is  $c_f = 3.7 \times 10^{-3}$ , which is comparable with the skin-friction coefficient calculated from a flat plate formulation ( $3.5 \times 10^{-3}$ ).

#### Part 2

Numerical simulations for the baseline submerged inlet have been performed for the freestream conditions given in Table 1. The exit back pressure of the diffuser is 99.75 kPa, which is equal to the

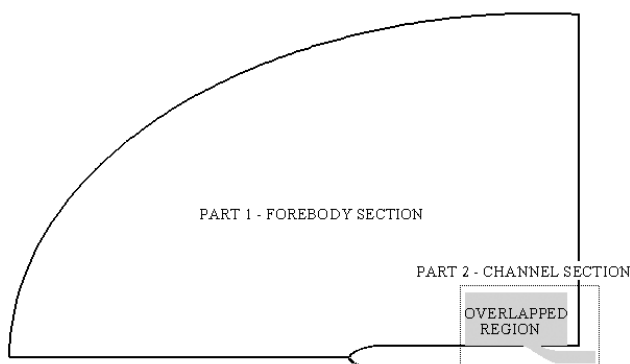
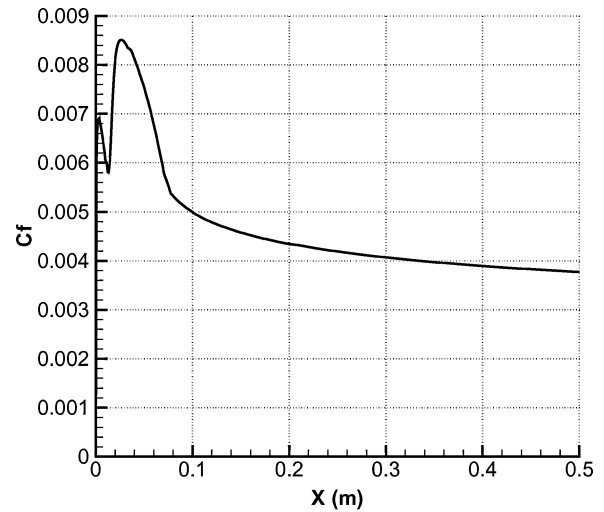
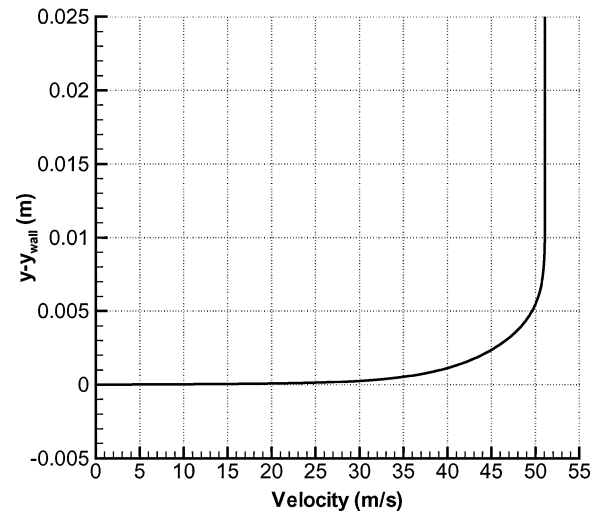


Fig. 10 Flow domain.



a) Skin-friction variation along the solid wall



b) Velocity profile at the end of the first domain

Fig. 11 Solutions of part 1.

freestream static pressure. On the basis of a one-dimensional inviscid analysis, this corresponds to a unit area mass flow rate of  $q = 0.25$ , where  $q$  is defined as  $q = \rho u / \rho^* u^*$  where  $\rho$  is the density,  $u$  is the velocity, and the superscript asterisk represents the sonic conditions.

Computational results are presented in terms of surface (Fig. 12) and volume (Fig. 13) streamlines along the channel section. In addition, velocity and total pressure contour plots at the exit plane of the inlet duct are given in Fig. 14. Surface streamline plots show the singularities in the flow domain; for example, a nodal point of attachment from which all the surface streamlines directed away is typically a stagnation point, a focus on the surface extends into the fluid as a concentrated vortex filament, and a saddle point on the wall is an indication of new stream surface originating at the wall.<sup>37,38</sup> Therefore, to detect crucial flow behavior in three dimensions, the surface streamline pattern in two dimensions is examined. The top view of the surface streamlines (Fig. 12a) shows a foci point of separation,  $F_S$ , on the upper part of the diffuser. Two line of separations,  $L_S$ , on both sides of the axis of symmetry merge to the  $F_S$ . Farther downstream along the duct, there is a saddle point  $S$ . The appearance of the focus point with a saddle point implies an existence of a central vortical core about which a coiled sheet is formed. The surface stemming from the line of separation acts as a barrier between the streamlines on its two sides.<sup>37</sup> The bottom view of the surface streamlines (Fig. 12b) does not show any singularity, which underlines that flow has minimal distortion near the lower duct wall. When the volume streamlines in Fig. 13 are examined,

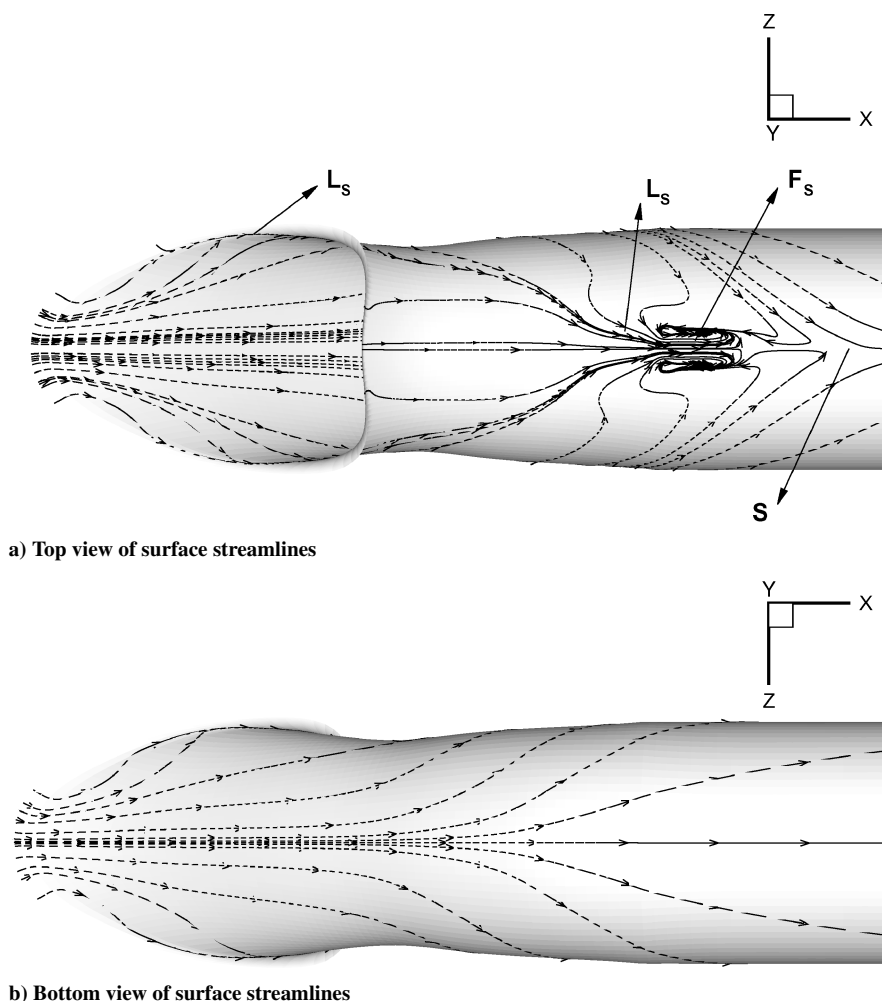


Fig. 12 Surface streamlines at channel walls.

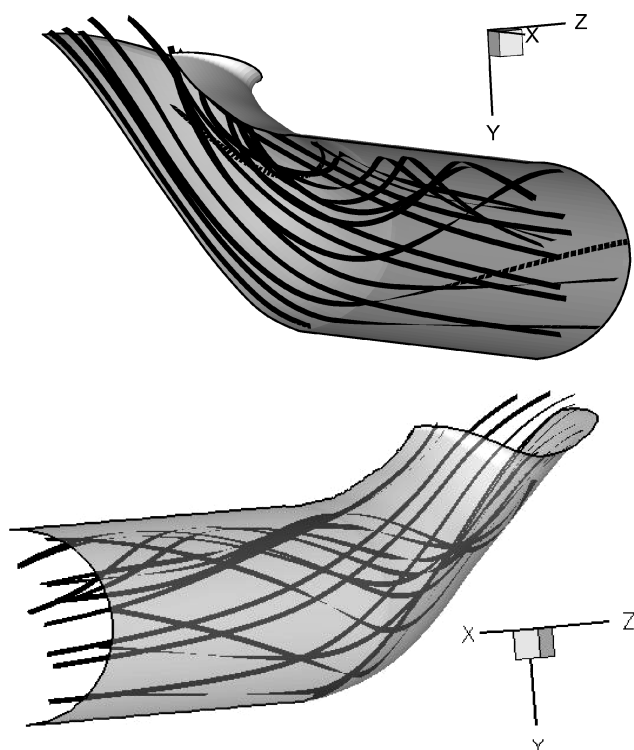


Fig. 13 Volume streamlines along the channel section.

the implications of the singularities seen on the surface streamline plots become more clear. The volume streamlines are very smooth near the lower duct, whereas they are twisted near the upper duct. It is apparent that flow distortion originates near the upper duct wall.

High total pressure occupying the central duct is swept to the side walls at the exit of the diffuser. The boundary layer on the upper duct thickens along the channel, yielding a low-velocity region near the exit of the channel. This low-velocity region corresponds to a low total pressure region in Fig. 14a. Although the change in total pressure at the exit cross section is within 1% only, the variation in velocity at the exit plane is almost 60%, indicating a high flow distortion (Figs. 14a and 14b).

#### Grid Sensitivity Analysis

It is required to compute the flow-domain solution many times during the optimization process. Both the objective function evaluation and the gradient calculation are performed by the flow solver. Therefore, it is critical to examine the accuracy of the solver and how much computational time it needs for our specific problem. Because each result is an approximate solution of nonlinear partial differential equations, there exist truncation errors in the flow domain solution. The truncation errors depend on the grid resolution. Hence, it is important to decide the grid size that is sufficient to solve the flow domain accurately and is small enough to save computational time. To be able to decide the sufficient number of grid points, grid sensitivity (truncation error) analysis for our specific problem is necessary. To determine the effects of truncation errors involved in the numerical analysis of the baseline inlet, a sequence of three grids of increasing resolution are prepared. Based on their grid density,

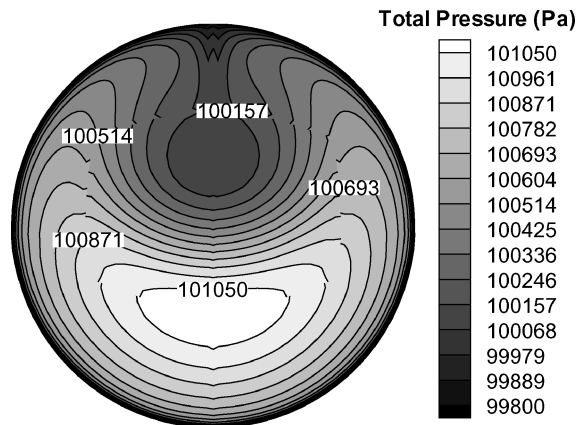
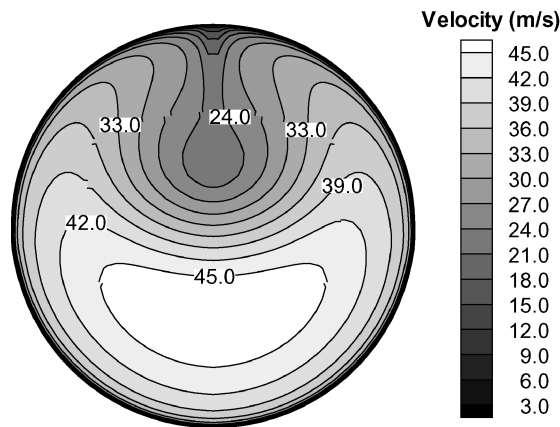
**Table 2** Grid sensitivity analysis for baseline inlet

Run	No. of grids	DC	SC	$\dot{m}$ , g/s
Coarse	76,224	0.593	0.094	26.52
Medium	473,600	0.523	0.101	27.56
Fine	2,542,592	0.510	0.090	27.98

**Table 3** CPU time necessary for each grid resolution

Run	WCT, <sup>a</sup> h	Processors	Courant–Friedrichs–Lewy
Coarse	8	16	1
Medium	16	64	1
Fine	60	128	5

<sup>a</sup>Computations performed on NCSA Linux cluster with Pentium III processors (1 GHz).

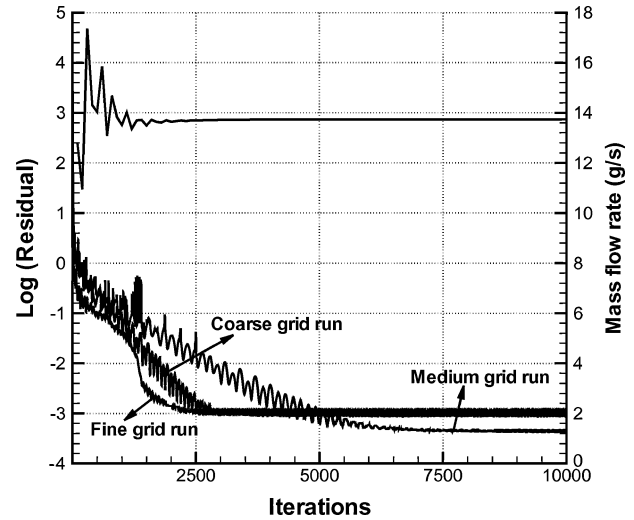
**a) Total pressure contour plots****b) Velocity contour plots****Fig. 14** Contour plots at the exit cross section.

they are named as coarse, medium, and fine grid. The flow-domain solution for each grid size is obtained, and the objective functions of the optimization (distortion and swirl indices) are computed. Table 2 shows the number of grid points and corresponding objective function values for coarse, medium, and fine grid run definitions. When the resulted values of distortion and swirl indices in Table 2 are compared, it is seen that the difference between fine and medium grid solutions are 2.5% for distortion index and 11.5% for swirl index, that is, the truncation error can be considered as acceptably small for the baseline inlet. Therefore, in our subsequent calculations a grid of medium size with approximately 500,000 nodes is used.

During the grid sensitivity analysis, the input parameters of the flow solver are kept the same except for the Courant number and the number of processors to speed up the computation (Table 3). The wall clock time (WCT) for the coarse grid run is 8 h with 16 processors if the local Courant number is chosen to be 1, WCT for

**Table 4** Design space

Parameter	Value
Height, mm	2.08 to 12.48
Length, mm	4.16 to 24.96
Incidence angle, deg	−20 to 20

**Fig. 15** Convergence history for each grid resolution.

the medium grid is 16 h with 64 processors, and WCT for the fine grid increases to approximately 60 h with 128 processors and a local Courant number of 5. The grid sensitivity analysis was performed at the National Center for Supercomputing Applications (NCSA's) IA32 Linux cluster Platinum. Convergence of each run is decided according to the residual history in addition to the mass flow rate at the inlet discharge. Although, convergence is reached earlier, a total of 10,000 iterations for each run definition is performed (Fig. 15).

The flow solutions for the fine and coarse grid resolution are given in Fig. 16 for comparison purposes. Figures 16a, 16b, and 16c show the grid, velocity, and total pressure contour plots, respectively, at the exit cross section of the inlet. The left-half of Figs. 16 show the fine grid solution and right-half the coarse grid solution. The general pattern is the same for both resolutions. There is a low-energy fluid on the upper duct indicating the flow distortion.

### Trade Study

A trade study is an essential prerequisite for an automated design optimization. The purpose of the trade study is to gain physical insight into the effect of specific types of shape deformations on the optimization parameters, that is, specific to our study distortion and swirl indices. The results of the trade study may be positive, that is, shapes are found that reduce either distortion index or swirl index or both, or negative, that is, the opposite. Nevertheless, the results lead to both understanding and provide insight to the type of shape changes to be considered with automated design optimization. Thus, for each design variable, namely, height, length, and incidence angle of the fin, a trade study is performed. The range of design variables is the same with the design space of the optimization study, and it is tabulated in Table 4. The sensitivity analysis for each design variable is performed by keeping two design variables constant while varying the design variable under consideration between upper and lower limits of the design space. The results of the sensitivity analysis for any design variable highly depend on the constant values chosen for the other two design variables. We selected these values according to an earlier optimization study conducted with the weighted sum approach.<sup>30</sup>

### Influence of Fin Orientation

First, the influence of the fin orientation on distortion and swirl indices is investigated. A total of nine runs with incidence angle



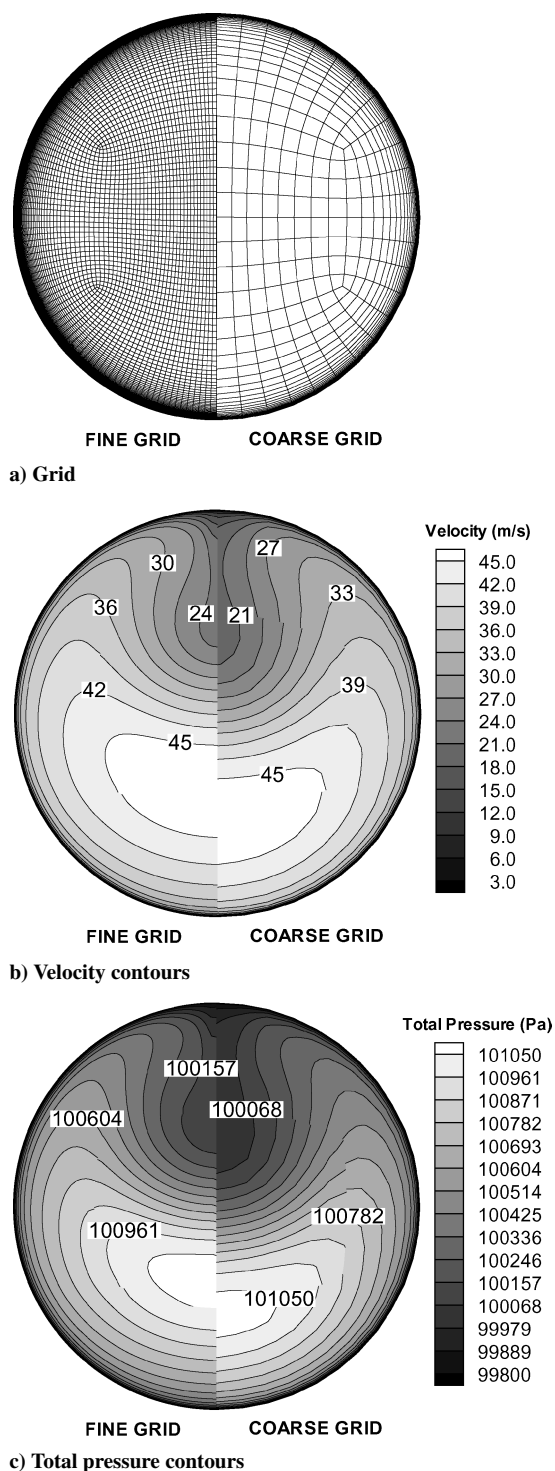


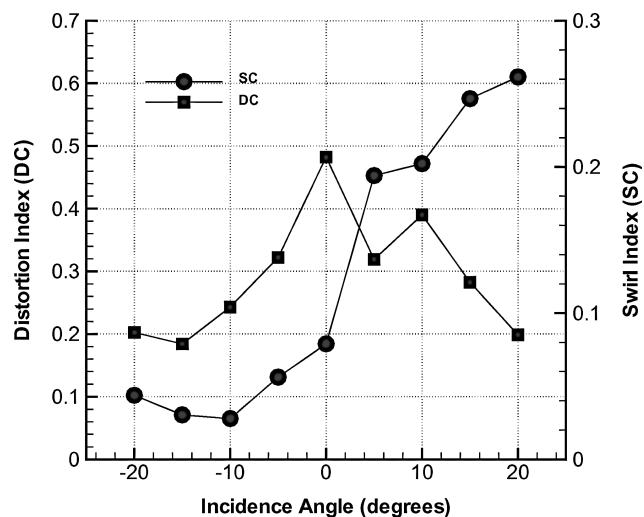
Fig. 16 Flow solution at the inlet discharge.

between  $-20$  and  $+20$  deg is performed while keeping the height and length of the fin at 10.4 and 20.8 mm, respectively. Table 5 displays the sensitivity of the distortion and swirl indices to fin orientation. As shown in Table 5, the minimum distortion index is obtained at  $-15$  deg; however, a distortion index value very close to this minimum value is obtained also for  $+20$  deg. Maximum distortion index, which is still lower than the distortion index of the baseline inlet, is seen at the neutral position of the fin, that is, at 0 deg.

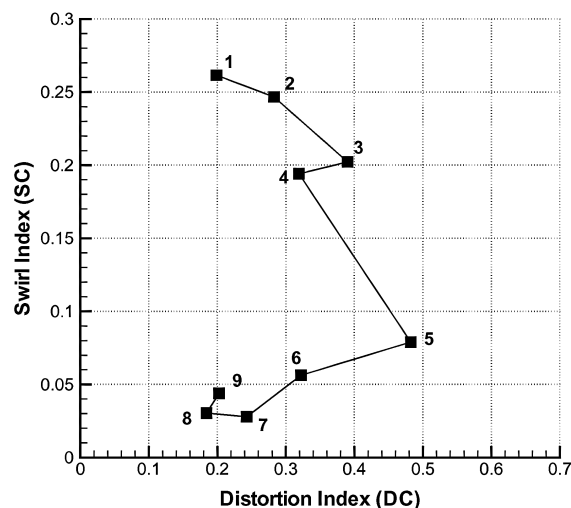
As the angle of the fin increases from  $-20$  deg to its neutral position, first a slight decrease then a substantial increase in distortion index is observed (Fig. 17a). After the maximum peak is reached at the neutral position of the fin, a decrease is seen as the angle is

Table 5 Orientation sensitivity

Design	$\gamma_{fin}$ , deg	DC	SC
1	+20	0.199	0.262
2	+15	0.283	0.247
3	+10	0.390	0.202
4	+5	0.319	0.194
5	0	0.482	0.079
6	-5	0.322	0.056
7	-10	0.243	0.028
8	-15	0.184	0.030
9	-20	0.203	0.044



a) Variation of distortion and swirl indices with incidence angle



b) Distortion index vs swirl index

Fig. 17 Sensitivity to fin orientation.

further increased, suggesting a bell-shape curve with two minima. The swirl index has an increasing trend on both sides of its minimum (Fig. 17a). The minimum and maximum swirl indices are seen at  $-10$  and  $+20$  deg of incidence, respectively. Figure 17b shows the variation of distortion with swirl index. The node numbers correspond to the data in Table 5. Designs 7 and 8 dominate the other designs under the conditions of fixed  $h_{fin}$  and  $l_{fin}$ . Design 7 has the smallest swirl index, whereas design 8 has the smallest distortion index. Given the estimated uncertainties in the computation of distortion and swirl indices using the medium grid, that is, approximately 3 and 12%, respectively, it is evident that designs 7 and 8 have comparable swirl, but design 8 has a demonstrably lower distortion. The other solutions are larger than these two cases either in distortion index or in swirl index or in both.

**Table 6** Height sensitivity

Design	$h_{fin}$ , mm	DC	SC
1	12.48	0.589	0.128
2	10.40	0.482	0.079
3	8.32	0.505	0.079
4	6.24	0.578	0.076
5	4.16	0.610	0.089
6	2.08	0.537	0.104

**Table 7** Length sensitivity

Design	$l_{fin}$ , mm	DC	SC
1	24.96	0.508	0.138
2	20.80	0.482	0.079
3	16.64	0.302	0.065
4	12.48	0.461	0.077
5	8.32	0.556	0.092
6	4.16	0.590	0.089

#### Influence of Fin Height

The height of the fin is varied between 2.08 and 12.48 mm while the length and the incidence angle are kept at 20.8 mm and 0 deg, respectively. As indicated in Table 6, distortion and swirl indices are not as sensitive to the height change as to the incidence change. The tabulated values show that the distortion index changes between 0.48 and 0.61, which is one third of the variation seen by incidence angle change. Maximum and minimum distortions are reached for the fin heights of 4.16 and 10.4 mm, respectively. The swirl index is minimum at 6.24-mm fin height. As is can be seen in Fig. 18a, swirl increases after a height of 10.4 mm and before 4.16 mm; however, the variation is negligibly small. The curve is almost flat between 5 and 10.4 mm. Figure 18b, distortion vs swirl, suggests that designs 2 and 4, corresponding to the fin height of 10.4 and 6.24 mm, respectively, give the nondominated solutions under the condition of fixed  $l_{fin}$  and  $\gamma_{fin}$ . As show in Fig. 18, designs 2–4 yield a slight decrease in swirl while distortion increases. When the fin height is lowered to 2.08 mm, design 6, both swirl and distortion increase.

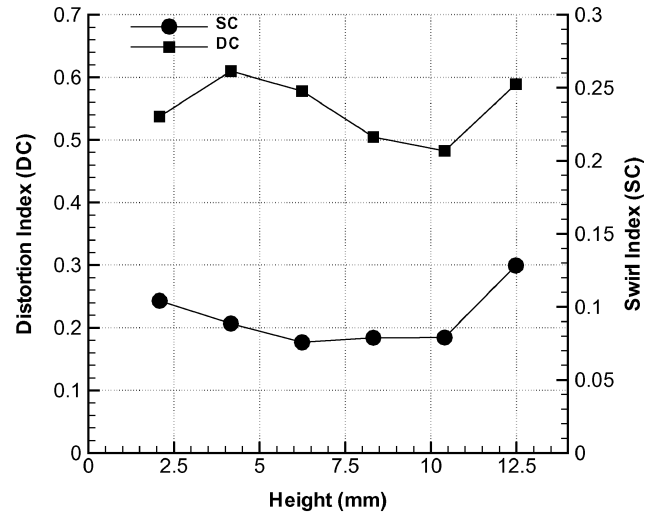
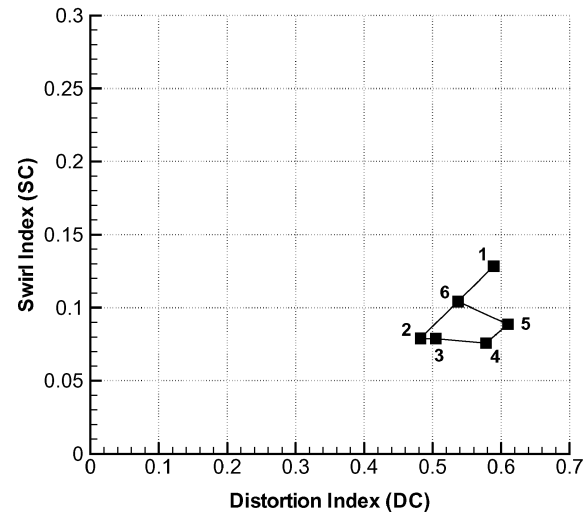
#### Influence of Fin Length

Similar to height sensitivity analysis described in the preceding subsection, fin length is varied to examine its effect on the distortion and swirl characteristics. The range of the fin length is chosen to be between 4.16 and 24.96 mm. The height and incidence angle of the fin are kept constant at 10.4 mm and 0 deg, respectively. The distortion and swirl indices are tabulated in Table 7. It is seen that the minimum distortion and swirl is obtained at length of 16.64 mm. Both increase or decrease from this length, 16.64 mm, yields an increase in distortion and swirl indices. When the fin length is changed, a 40% improvement in distortion and swirl is gained.

Distortion and swirl variation by fin length can be seen in Fig. 19a. The minimum distortion and swirl indices coincide at 16.64 mm, as shown in Fig. 19a. Figure 19b shows the variation of flow distortion with flow swirl. Design 1 corresponds to the maximum flow swirl. The swirl index declines abruptly to half of its value in design 2, and it continues to decrease in design 3. The distortion index decreases slightly for design 2 and sharply for design 3. An increase in both swirl and distortion index is observed for designs 4 and 5. At design 6, a slight decrease seen in swirl but distortion still increases. As is clearly seen in Fig. 19, design 3 is the nondominated solution among the six design solutions obtained by varying the fin length. It refers to the fin length of 16.64 mm. Below this length, flow distortion and swirl increases. Above this length, a larger swirl is created.

#### Optimization

To find the Pareto set for a design optimization incorporating all three design variables, a series of optimization runs for a set of  $\varepsilon$  values are performed. There are 12 optimization runs, each

**a) Variation of distortion and swirl indices with height****b) Distortion index vs swirl index****Fig. 18** Sensitivity to fin height.

of which corresponds to a different  $\varepsilon$  value in the range between 0.025 and 0.300. This range is decided based on the trade study already explained. For each design variable, one step is taken based on the user-specified step size, and the gradient is calculated with forward finite differencing using the new function value one step away from the design point and at the design point. The initial point selection is done based on the swirl index values found in the trade study. According to the sensitivity analysis performed for incidence angle, the distortion index has two minima at two opposite directions. The one with the positive incidence angle has a higher swirl value. The optimization must be initiated with this design point to avoid the optimizer being locally trapped in one local minimum. Because the solution space containing design points with high swirl values will be eliminated for smaller constraint values, there is no such danger for an initial design point having large swirl. All of the optimization runs are, therefore, initiated from the upper bound of the design space, that is,  $h_{fin} = 12.064$  mm,  $l_{fin} = 24.128$  mm, and  $\gamma_{fin} = +19$  deg. If the starting point is not in the feasible region, a feasible point will be generated based on the constraint value. Hence, the first step of the optimization is to check if the starting point is feasible or not. In case it is in the infeasible region, CFSQP generates an acceptable feasible design point. After the design point to start the optimization is found, the next four flow computations are performed to compute the gradients with respect to our three design variables. Table 8 summarizes the feasible initial points found by CFSQP for every  $\varepsilon$  value under investigation. As it is seen for  $\varepsilon$  of 0.025, no feasible design point could be found.

**Table 8** Feasible initial point for each  $\varepsilon$ 

Run	$\varepsilon \times 1000$	$h_{fin}$ , mm	$l_{fin}$ , mm	$\gamma_{fin}$ , deg	SC
1–2	300–275	12.064	24.128	+19	0.275
3–9	250–100	12.064	4.16	–20	0.078
10–11	75–50	12.064	17.328	–20	0.033
12	25	N/A	N/A	N/A	N/A

**Table 9** Optimization summary

Run	$\varepsilon \times 1000$	$h_{fin}$ , mm	$l_{fin}$ , mm	$\gamma_{fin}$ , deg	DC	SC
1	300	11.886	23.504	+17.781	0.039	0.279
2	275	11.903	23.504	+17.781	0.048	0.270
3–9	250–100	12.064	14.144	–20	0.588	0.078
10–11	75–50	9.568	19.029	–10.25	0.196	0.030

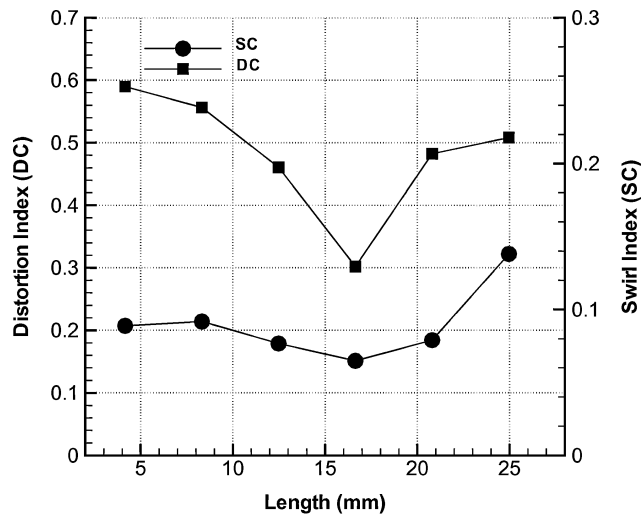
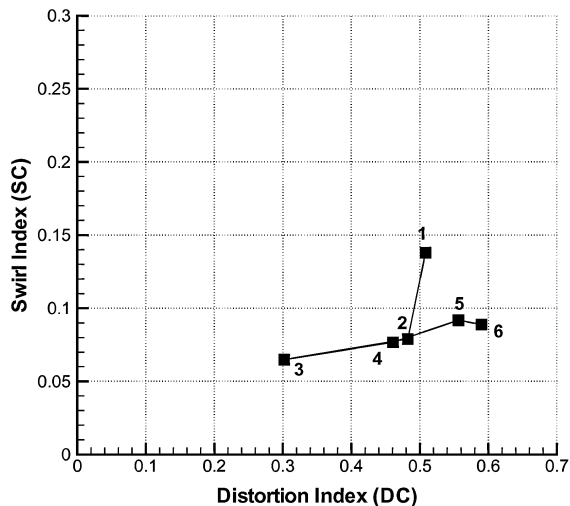
**a)** Variation of distortion and swirl indices with length**b)** Distortion index vs swirl index**Fig. 19** Sensitivity to fin length.

Table 9 summarizes optimum points found for each optimization run. During the construction of the Pareto optimal set, inferior points from the tabulated summary are omitted. Optimization runs 3–9 are redundant because they are dominated by the solutions of the run numbers 1, 2, and 10–11. However, when the optimization run numbers 10 and 11 are examined, another four solutions in the Pareto set are found. Similarly, run numbers 1 and 2 add two more solutions to the Pareto set. Table 10 shows the swirl and distortion indices

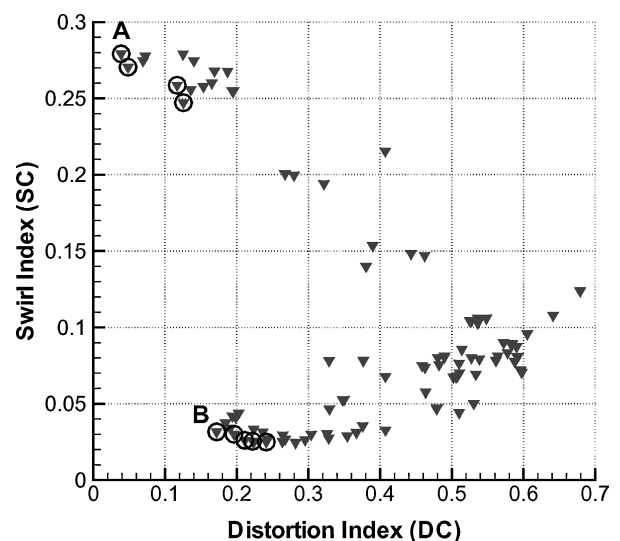
of each inlet design in Pareto optimal set. The reason for not being able to detect these solutions is simply the constraint values we have chosen, that is, the chosen increment in  $\varepsilon$  is large. The difference in constraint values for the Pareto optimal solutions are very close to the same constraint value and to each other (Table 10). It is neither practical nor necessary to fine tune the specified constraint values within a small region because the uncertainty level of the optimization process is higher than the possible improvement that will be obtained by fine tuning. Moreover, in the optimization process, it is likely that additional better design points will be detected by the optimizer. Figure 20 shows the Pareto solution set marked with circles. The Pareto optimal is scattered in two separate regions. In region A, the flow has low distortion index ranging between 0.04 and 0.13 with high swirl. In region B, it has low distortion index between 0.17 and 0.24 with low swirl. The optimum inlets have fin height and fin length in the range of 9–12 and 18–24 mm, respectively. The incidence angle principally determines the value of the swirl index. It is high when the fin is rotated 20 deg in the counterclockwise

**Table 10** Pareto optimal set

DC	SC	$h_{fin}$ , mm	$l_{fin}$ , mm	$\gamma_{fin}$ , deg
<i>Baseline</i>				
0.523	0.101			
<i>Subset A</i>				
0.039	0.279	11.886	23.504	17.781
0.048	0.270	11.903	23.504	17.781
0.117	0.256	11.820	24.128	17.781
0.126	0.247	12.064	21.025	16.375
<i>Subset B</i>				
0.172	0.032	10.502	24.128	–20.000
0.196	0.030	9.568	19.029	–10.250
0.211	0.026	10.702	18.658	–15.125
0.222	0.026	10.702	18.658	–14.125
0.241	0.025	11.283	20.728	–19.000

**Table 11** Grid sensitivity analysis for optimum inlets

Grid	No. of grids	DC	SC
<i>Inlet A</i>			
1	457,728	0.144	0.273
2	4,534,272	0.130	0.273
<i>Inlet B</i>			
1	457,728	0.172	0.032
2	2,977,920	0.287	0.028
3	3,858,432	0.278	0.028

**Fig. 20** Approximate Pareto optimal solution.

direction, and it is low when it is rotated 20 deg in the clockwise direction.

The Pareto set found through the optimization study is in fact an approximate Pareto set due to the uncertainty involved in each flow solution. Note that the aim of our optimization methodology is to find an approximate Pareto set rather than the refined Pareto set. Given the computational expense of the function evaluation step of our design problem, it is not feasible to investigate the uncertainty level in every iterate of the line search. Instead the global pattern of the Pareto front is sought, and only the uncertainty level in the Pareto set is investigated at the end of the optimization. It is assumed that

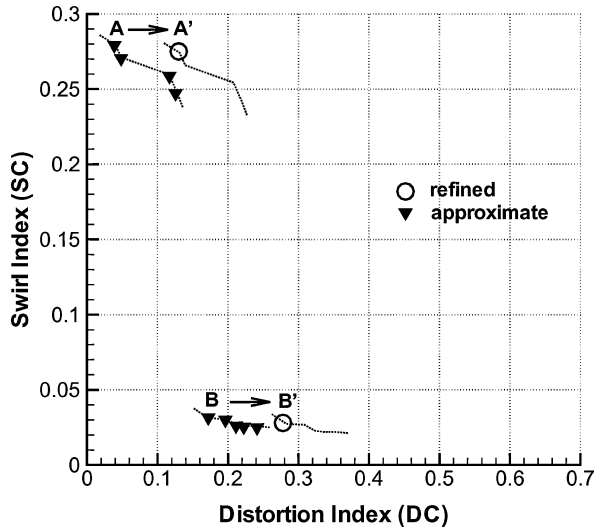


Fig. 21 Refined Pareto optimal solution.

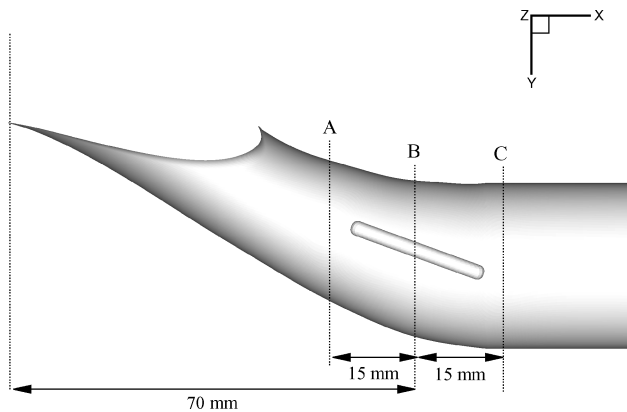


Fig. 22 Optimum inlet B.

the structure of the real Pareto front is similar to the approximate Pareto front found in the optimization (Fig. 21).

#### Grid Sensitivity Analysis for the Optimum Inlets

Optimization study gives two Pareto optimal subsets (subsets A and B given in Table 10) for which flow behavior is different. One set of inlet designs displays high swirl values, whereas the other possesses low swirl values compared to the baseline inlet. The change in flow behavior brings into question the accuracy of the optimum inlet solutions, and it necessitates new grid sensitivity analyses for the optimum inlets found. Thus, one optimum inlet is selected from each Pareto optimum subset, and a truncation error analysis is performed for each of these design points. These inlet designs are called optimum inlet A and B according to the subset they are chosen from. Optimum inlet A has  $h_{fin} = 11.886$  mm,  $l_{fin} = 23.504$  mm, and  $\gamma_{fin} = 17.781$  deg. Optimum inlet B has  $h_{fin} = 10.502$  mm,  $l_{fin} = 24.128$  mm, and  $\gamma_{fin} = -20$  deg. Table 11 shows the objective function values calculated with different grid resolutions for both optimum inlets A and B. The resolution is specifically increased in the region downstream of the fin. For optimum inlet A, solutions with two sequences of grid resolutions are obtained. It is observed that swirl is almost insensitive to the grid resolution, but the distortion index has decreased by 11%. For optimum inlet B, three sequences of grid resolutions are investigated. Distortion and swirl indices for this inlet are converged to 0.278 and 0.028, respectively. Note that the refined grid solutions A' and B' in Fig. 21 remain nondominated.

#### Analyses of Optimum Inlets

In Fig. 22, optimum inlet B is marked with three constant  $x$  locations as shown. Stations A, B, and C are located upstream, in the middle, and downstream of the fin, respectively. The inertial forces due to the duct curvature creates a swirl in counterclockwise direction on the right-half of the inlet duct looking downstream for the baseline inlet (Fig. 23a). The schematics of flow swirl at station B for optimum inlets A and B are shown in Figs. 23b and 23c, respectively. A fin protrusion with a positive incidence angle, as in the case of optimum inlet A, creates a higher pressure region over the upper surface of the fin. The pressure differential between lower and upper surfaces of the fin causes the formation of a tip vortex with counterclockwise circulation, which, therefore, accentuates the swirl, although creating a more axisymmetric flowfield (and hence, lower distortion) (Fig. 24). A fin protrusion with a negative incidence angle, however, creates lower pressure region on the upper surface of the fin. This results in a tip vortex formation in the clockwise direction, opposite to the swirl direction of the baseline inlet. The tip vortex on the right of the inlet is clockwise looking downstream. It is shown in Fig. 25 (counterclockwise on the left looking upstream).

Pressure distributions along the duct wall at each station are shown in Fig. 26. Figures 26 clearly indicate that flow swirl and distortion are basically a consequence of lateral pressure variation across the duct bend rather than longitudinal pressure distribution along the

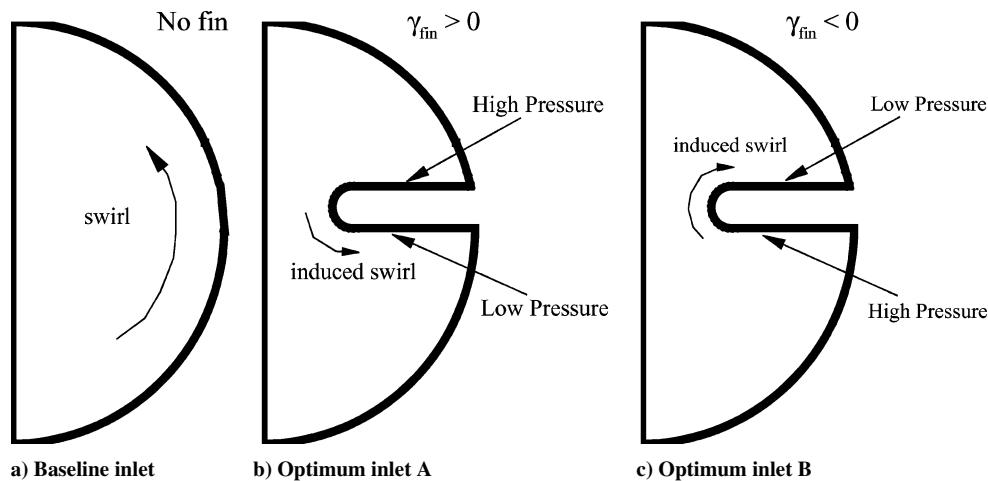
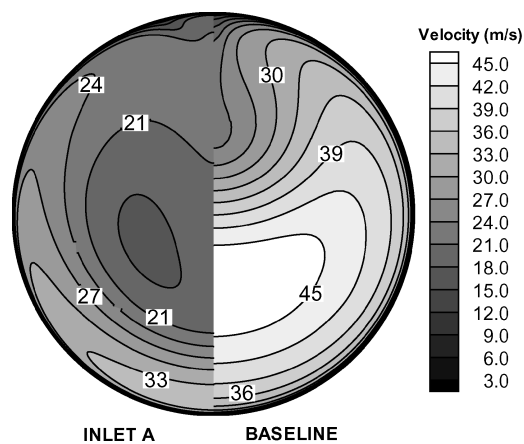
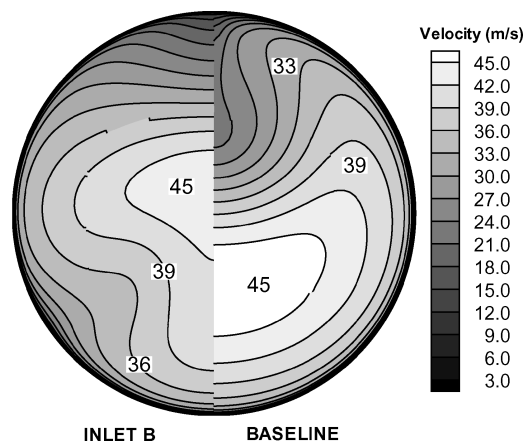


Fig. 23 Schematic of flow swirl.



a) Optimum inlet A



b) Optimum inlet B

Fig. 24 Velocity contours at inlet discharge.

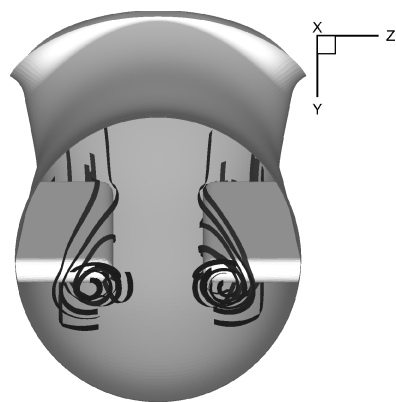
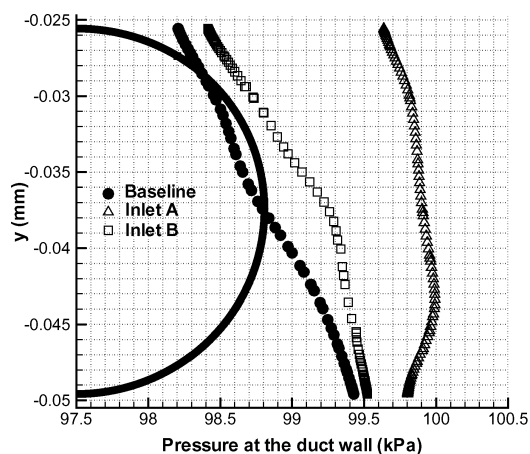
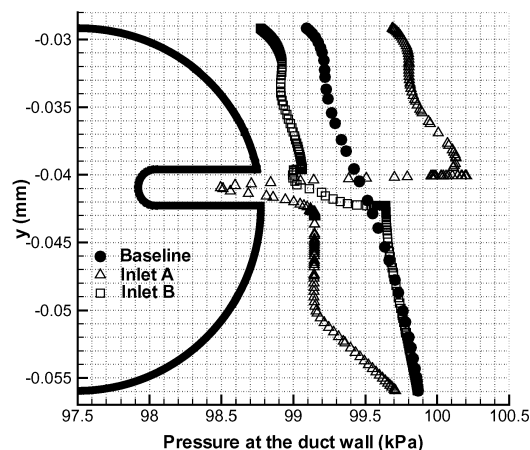


Fig. 25 Tip vortex, optimum inlet B, looking upstream.

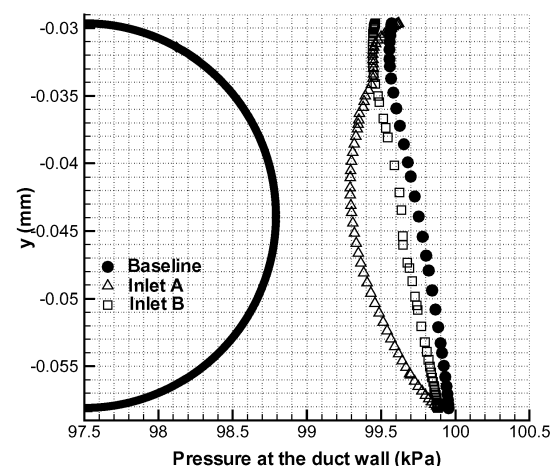
duct. At station A (Fig. 26a), for baseline inlet and optimum inlet B, there is a large pressure differential between the lower and the upper duct that drives the counterclockwise secondary flow. At station C (Fig. 26c), the pressure variation is almost constant and comparable for the baseline and optimum inlet B. At station B (Fig. 26b), the addition of a fin with negative incidence angle lowers the pressure on the upper duct, whereas the lower duct pressure is comparable with that of the baseline inlet. The pressure differential between the lower and upper surfaces of the fin creates a tip vortex opposite to the flow swirl direction observed in the baseline inlet. On the other hand, flow behaved differently for optimum inlet A. It has smaller pressure variation along the duct wall at station A (Fig. 26a) and larger pressure variation at station C (Fig. 26c) compared to the other two inlets. At station B, the upper duct has higher pressure than lower duct, resulting in a tip vortex in the direction of the flow swirl seen in the baseline inlet.



a) Station A



b) Station B



c) Station C

Fig. 26 Pressure distribution along duct wall.

## Conclusions

A multi-objective optimization study for a low subsonic submerged inlet is conducted using the trade-off method. The figures of merit of the optimization are chosen to be the measures of flow uniformity over the exit cross section of the inlet, namely, the flow distortion and swirl indices, whereas the design variables are the geometric parameters defining the fin protrusion introduced on the inlet walls, namely, fin height, length, and orientation.

1) A trade study for each design variable shows that the orientation of the fin has a strong influence on the objective functions, especially on the swirl index. Flow swirl increases with positive angle of incidences, whereas flow distortion has a peak in the fin neutral position ( $\gamma_{fin} = 0$  deg) and it decreases as the fin rotates

around the fin center in either direction. For fin lengths less than 17 mm and for fin heights less than 10 mm, the distortion index drops, whereas the swirl index is found to be insensitive to both variables. Increasing height and length of the fin further results in diverging from the optimum values.

2) The Pareto set constructed by minimizing the distortion index while restricting the swirl index yields an irregular and discontinuous Pareto front. The Pareto set is composed of four design points of low distortion but high swirl and five other design points of low distortion and low swirl. A jump from the first set to the second set yields a decrease in swirl index but an increase in distortion index. As a result, the inlet designer has two options: an inlet design 1) with high swirl but low distortion or 2) with low swirl but higher distortion.

3) The principal benefit of the fin is the generation of a large tip vortex within the inlet, which substantially modifies the flowfield. The fins are conceptually different from the conventional boundary-layer vortex generators used in previous studies because they affect the entire flowfield (both boundary layer and inviscid core).

4) A grid sensitivity analysis is conducted for selected two inlet designs from each Pareto optimal set. It is observed that, with inlet design A, distortion index decreases by 70% at the expense of a substantial increase in swirl index as compared to that of baseline inlet. For inlet design B, decreases of 45 and 70% over that of baseline inlet are seen in distortion and swirl indices, respectively.

Because flow swirl may damage compressor blades, physically leading to engine surge, inlet design B with low flow swirl may be preferable for a jet turbine engine. On the other hand, for a ramjet engine, flow swirl may help to increase turbulence levels and fuel mixing, to promote flame stabilization, and to enhance flame propagation by creating a central recirculation zone. Thus, inlet design A with large flow swirl may be desirable for a ramjet engine.

### Acknowledgments

This research is supported by the National Science Foundation under Grant NSF-CTS-0121058 monitored by Frederica Darema, Chuan Chen, and Michael Plesniak. The authors would like to thank Alexei Kotelnikov, Unix system administrator of Rutgers University, for his valuable support. Supercomputer resources were provided by the National Center for Supercomputer Applications, University of Illinois at Urbana-Champaign.

### References

- Huenecke, K., "Air Intakes," *Jet Engines, Fundamentals of Theory, Design and Operation*, 2nd ed., Motorbooks International, Osceola, WI, 1998, Chap. 3, pp. 44–86.
- Seddon, J., and Goldsmith, E. L., *Intake Aerodynamics*, 1st ed., AIAA Education Series, Collins Professional and Technical Books, AIAA, New York, 1985, Chaps. 1 and 11.
- Goldsmith, E. L., and Seddon, J., *Practical Intake Aerodynamic Design*, 1st ed., AIAA Education Series, Collins Professional and Technical Books, AIAA, New York, 1993, Chaps. 1 and 2.
- Treager, I. E., "Aircraft Gas Turbine Engine Technology," *Jet Engines, Fundamentals of Theory, Design and Operation*, 3rd ed., GLENCEO Aviation Technology Series, MacGraw-Hill, New York, 1995, Chap. 4, pp. 162–167.
- Bansod, P., and Bradshaw, P., "The Flow in S-Shaped Ducts," *Aeronautical Quarterly*, Vol. 23, May 1972, pp. 131–140.
- Povinelli, L. A., and Towne, C. E., "Viscous Analyses for Flow Through Subsonic and Supersonic Intakes," NASA TM 88831, Sept. 1986.
- Wellborn, S. R., Reichert, B. A., and Okiishi, T. H., "An Experimental Investigation of the Flow in a Diffusing S-duct," *Journal of Propulsion and Power*, Vol. 10, No. 5, 1994, pp. 668–675.
- Mayer, D. W., Anderson, B. H., and Johnson, T. A., "3D Subsonic Diffuser Design and Analysis," AIAA Paper 98-3418, July 1998.
- Frick, C. W., Davis, W. F., Randall, L. M., and Mossman, E. A., "An Experimental Investigation of NACA Submerged-Duct Entrances," NACA ACR-5120, Nov. 1945.
- Sacks, A. H., and Spreiter, J. R., "Theoretical Investigation of Submerged Inlets at Low Speed," NACA TN-2323, Aug. 1951.
- Thomas, A. N., "Inlets," *Tactical Missile Aerodynamics*, 1st ed., AIAA, New York, 1986, Chap. 4, pp. 129–167.
- Harper, D. K., Leitch, T. A., Ng, W. F., and Guillot, S. A., "Boundary Layer Control and Wall-Pressure Fluctuations in a Serpentine Inlet," AIAA Paper 2000-3597, July 2000.
- Reichert, B. A., and Wendt, B. J., "An Experimental Investigation of S-Duct Flow Control Using Arrays of Low-Profile Vortex Generators," AIAA Paper 93-0018, Aug. 1993.
- Reichert, B. A., and Wendt, B. J., "Improving Curved Subsonic Diffuser Performance with Vortex Generators," *AIAA Journal*, Vol. 34, No. 1, 1996, pp. 65–72.
- Anderson, B. H., Huang, P. S., Paschal, W. A., and Cavatorta, E., "Study on Vortex Flow Control of Inlet Distortion," *Journal of Propulsion and Power*, Vol. 8, No. 6, 1992.
- Guo, W. R., and Seddon, J., "The Swirl in an S-duct of Typical Air Intake Proportions," *Aeronautical Quarterly*, Vol. 34, May 1983, pp. 99–129.
- Seddon, J., "Understanding and Countering the Swirl in S-ducts: Tests on the Sensitivity of Swirl to Fences," *Aeronautical Journal*, Vol. 88, No. 874, April 1984, pp. 117–127.
- Knight, D. D., "Automated Optimal Design of Supersonic and Subsonic Diffusers Using CFD," *Proceedings European Congress on Computational Methods in Applied Sciences and Engineering*, The European Community on Computational Methods in Applied Sciences Center, CIMNE, Barcelona, Spain, Sept. 2000.
- Knight, D. D., "Automated Optimal Design Using CFD and High Performance Computing," *Lecture Notes in Computer Science*, Springer-Verlag, Berlin, Vol. 1215, 1997, pp. 198–221.
- Knight, D. D., "Application of Genetic Algorithms to High Speed Air Intake Design," *Von Kármán Institute for Fluid Dynamics Lecture Series Program*, Rept. VKI LS 2000-07, Vol. 1, Rhode Saint Genese, Belgium, May 2000.
- Zha, G. C., Smith, D., Schwabacher, M., Rasheed, K., Gelsey, A., Knight, D., and Haas, M., "High Performance Supersonic Missile Inlet Design Using Automated Optimization," *Journal of Aircraft*, Vol. 34, No. 6, 1997, pp. 697–705.
- Blaize, M., Knight, D. D., and Rasheed, K., "Automated Optimal Design of Two-Dimensional Supersonic Missile Inlets," *Journal of Propulsion and Power*, Vol. 14, No. 6, 1998, pp. 890–898.
- Blaize, M., Knight, D. D., Rasheed, K., and Kergeravat, Y., "Optimal Missile Inlet Design by Means of Automated Numerical Optimization," *Proceedings of the RTO Meeting 5*, RTO-MP-5, Paper 37, BP 25, Neuilly-Sur-Seine Cedex, France, pp. 37–1–37–9.
- Rasheed, K., Hirsh, H., and Gelsey, A., "A Genetic Algorithm for Continuous Design Space Search," *Artificial Intelligence in Engineering*, Vol. 11, No. 3, 1997, pp. 295–305.
- Bourdeau, C., Carrier, G., and Knight, D., "Three Dimensional Optimization of Supersonic Inlets," AIAA Paper 99-2108, June 1999.
- Carrier, G., Bourdeau, C., Knight, D., Kergeravat, Y., and Montazel, X., "Multi-Flight Condition Optimization of Three-Dimensional Supersonic Inlets," *Proceedings of the RTO Meeting 35*, RTO-MP-035, Paper 30, BP 25, Neuilly-Sur-Seine Cedex, France, pp. 30-1–30-10.
- Zhang, W., Knight, D., and Smith, D., "Automated Design of a Three Dimensional Subsonic Diffuser," *Journal of Propulsion and Power*, Vol. 16, No. 6, 2000, pp. 1132–1140.
- Lefantzi, S., and Knight, D. D., "Automated Design Optimization of a Three-Dimensional S-Shaped Subsonic Diffuser," *Journal of Propulsion and Power*, Vol. 18, No. 4, 2002, pp. 913–921.
- Deb, K., *Multiobjective Optimization Using Evolutionary Algorithms*, 1st ed., Wiley, West Sussex, England, 2001, Chaps. 2 and 3.
- Taskinoglu, E., Jovanovic, V., Elliot, G., and Knight, D. D., "Design Optimization for Submerged Inlets, Part II," AIAA Paper 2003-3926, June 2003.
- Messac, A., Ismail-Yahaya, A., and Mattson, C. A., "The Normalized Normal Constraint Method for Generating the Pareto Frontier," *Journal of the International Society of Structural and Multidisciplinary Optimization*, Springer, Vol. 25, No. 2, 2003, pp. 86–98.
- Lawrence, C., Zhou, J. L., and Tits, A. L., "User's Guide for CFSQP, A Code for Solving Constrained Nonlinear Optimization Problem, Generating Iterates Satisfying All Inequality Constraints," Inst. for Systems Research, Rept. TR-94-16r1, Univ. of Maryland, College Park, MD, April 1997.
- "Pro/Engineer User's Guide," Release 20, Parametric Technology Corp., Needham, MA, 1996.
- "GridPro/az3000 User's Guide and Reference Manual," Program Development Corp., White Plains, NY, 1998.
- "General Aerodynamic Simulation Program User Manual," Ver. 4.1+, Aerosoft, Inc., Blacksburg, VA, 1996.
- Schwartz, R. L., *Learning Perl*, 1st ed., O'Reilly and Associates, Inc., Sebastopol, CA, 1993.
- Tobak, M., and Peake, D. J., "Topology of Three-Dimensional Separated Flows," *Annual Review of Fluid Mechanics*, Vol. 14, 1982, pp. 61–85.
- Tobak, M., and Peake, D. J., "Topology of Two-Dimensional and Three-Dimensional Separated Flows," AIAA Paper 79-1480, July 1979.